Acta Oceanol. Sin., 2015, Vol. 34, No. 9, P. 43–57
DOI: 10.1007/s13131-015-0737-1
http://www.hyxb.org.cn
E-mail: hyxbe@263.net

Evaluation of the simulation capability of the Wavewatch III model for Pacific Ocean wave

BI Fan[1, 2], SONG Jinbao[3]*, WU Kejian[2, 4], XU Yao[1]

[1] Key Laboratory of Ocean Circulation and Waves, Institute of Oceanology, Chinese Academy of Sciences, Qingdao 266071, China

[2] College of Physical and Environmental Oceanography, Ocean University of China, Qingdao 266100, China

[3] Ocean College, Zhejiang University, Hangzhou 310058, China

[4] Key Laboratory of Physical Oceanography (Ocean University of China), Ministry of Education, Qingdao 266003, China

Received 31 October 2014; accepted 23 March 2015

©The Chinese Society of Oceanography and Springer-Verlag Berlin Heidelberg 2015

Abstract

Wave climate analysis and other applications for the Pacific Ocean require a reliable wave hindcast. Five source and sink term packages in the Wavewatch III model (v3.14 and v4.18) are compared and assessed in this study through comprehensive observations, including altimeter significant wave height, advanced synthetic aperture radar swell, and buoy wave parameters and spectrum. In addition to the evaluation of typically used integral parameters, the spectra partitioning method contributes to the detailed wave system and wave maturity validation. The modified performance evaluation method (PS) effectively reduces attribute numbers and facilitates the overall assessment. To avoid possible misleading results in the root mean square error-based validations, another indicator called HH (indicating the two authors) is also calculated to guarantee the consistency of the results. The widely used Tolman and Chalikov (TC) package is still generally efficient in determining the integral properties of wave spectra but is physically deficient in explaining the dissipation processes. The ST4 package performs well in overall wave parameters and significantly improves the accuracy of wave systems in the open ocean. Meanwhile, the newly published ST6 package is slightly better in determining swell energy variations. The two packages (ACC350 and BJA) obtained from Wavewatch III v3.14 exhibit large scatters at different sea states. The three most ideal packages are further examined in terms of reproducing wave-induced momentum flux from the perspective of transport. Stokes transport analysis indicates that ST4 is the closest to the NDBC-buoy-spectrum-based transport values, and TC and ST6 tend to overestimate and underestimate the transport magnitude, respectively, in swell mixed areas. This difference must be considered, particularly in air–wave–current coupling research and upper ocean analysis. The assessment results provide guidance for the selection of ST4 for use in a background Pacific Ocean hindcast for high wave climate research and China Sea swell type analysis.

Key words: Wavewatch III, evaluation, Pacific Ocean, source and sink term packages, wave-induced flux, Stokes transport

Citation: Bi Fan, Song Jinbao, Wu Kejian, Xu Yao. 2015. Evaluation of the simulation capability of the Wavewatch III model for Pacific Ocean wave. Acta Oceanologica Sinica, 34(9): 43–57, doi: 10.1007/s13131-015-0737-1

1 Introduction

Ocean wave modeling is mainly based on energy density spectrum evolution. Possible physical processes and tunings are represented as source terms as follows:

$$S = S_{\text{in}} + S_{\text{nl}} + S_{\text{dis}} + \cdots , \tag{1}$$

in which the most general terms are the wind input (S_{in}) to absorb energy from the atmosphere, nonlinear wave–wave interaction (S_{nl}) to distribute energy in the spectra, and dissipation (S_{dis}) to represent white capping, wave-turbulence interaction, and others (Kalantzi et al., 2009). Inter-comparisons of different models are often conducted before conducting coastal and oceanic wave simulations. Padilla-Hernández et al. (2004) compared the performance of SWAN, WAM, and Wavewatch III (WWIII) in super storm cases. Ortiz-Royero and Mercado-Irizarry (2008) compared the performance of SWAN and WWIII in the North Atlantic Basin during summertime, and Jiang et al. (2010) assessed SWAN and WWIII wave parameters in monsoon and typhoon cases in Northern South China Sea. Hanson et al. (2009) systematically evaluated WAM, WWIII (v2.22), and WAVAD in the Pacific Ocean, and both wind-sea and swell (young and mature) partitions were compared. All these studies confirmed the capability of WWIII to provide generally good results with different wind forces in deep water waves.

Wave models have been developed in the past ten years, and numerous observation-based physical processes, particularly dissipation terms, have been implemented. Some of them can be found in the WWIII model. Their applications, together with the widely used default Tolman and Chalikov (TC) source term, cov-

Foundation item: The National High Technology Research and Development Program (863 Program) of China under contract No. 2013AA122803; the Strategic Priority Research Program of the Chinese Academy of Sciences under contract No. XDA11010104.
*Corresponding author, E-mail: songjb@zju.edu.cn

er research in many areas. For example, Dodet et al. (2010) employed the package of Ardhuin et al. (2010) in version 3.14 for the analysis of wave climate variability in the North–East Atlantic Ocean; the coupled atmosphere–wave modeling in a 29a global wave simulation adopted the TC (1996) package (Fan et al., 2012). A global wave parameter database for geophysical applications was produced based on improved source term parameterizations (Rascle et al., 2008; Rascle and Ardhuin, 2013). Most modeling studies evaluated the capability of their model setups by buoy or satellite observations and have reported acceptable accuracy results. However, when WWIII is selected in applications, the source term scheme to be used is not often indicated. Among the limited studies on this topic, Kalantzi et al. (2009) evaluated the performance of dissipation parameterizations in WWIII (v2.22) by using WAM3 and TC source term packages; they pointed out that (1) both packages are unable to perform adequately when the areas are mostly affected by swell and (2) considering only integral wave parameters does not provide information on inherent physical characteristics. Ardhuin et al. (2010) promoted semi-empirical dissipation source functions and presented an improvement to the previous Bidlot et al. (2005) revision. Rascle and Ardhuin (2013) further improved this source term package (switch called ST4 in WWIII v4.18) and obtained better results than those of TC packages.

We are mainly interested in the Pacific Ocean, the China Sea wave climate, and related coupling and mixing. A more suitable setup is required in the hindcast run. The newly published WWIII v4.18 provides many source term packages, five of which are selected and assessed in the Pacific Ocean. The method developed by Hanson et al. (2009) to facilitate selection of a wave modeling technology for multi-decade hindcast is modified and employed in our assessment. In this method, both wind-sea and swell components are considered, and the independent spectral values can be downscaled into indexes to yield overall information. To reduce possible bias in root mean square error (*rmse*)-based model validations, another index of Mentaschi et al. (2013) is utilized to guarantee the reliability of the results. Section 2 introduces the selected source/sink packages. Section 3 describes the model setup of the experiments, preprocessing of observation data for validations, and related calibration of wind forcing; the two assessment methods are also introduced in this section. Detailed wave simulation results with both integrated wave parameters and partitioned wave systems are shown in Section 4. Wave-related momentum flux and wave-induced transport in the upper ocean are compared in Section 5 to facilitate the following work in upper ocean energy transfer. Lastly, the conclusions and discussions are presented in Section 6.

2 Wavewatch III version 4.18 source/sink packages

In WWIII, the source terms of input and dissipation are regarded as packages. Recent implementations of source/sink terms that consider more physical processes for deep ocean waves are the main focus of this study. Among all the packages, the following four options are examined (leading to five experiments).

(1) The default TC (1996) package, which consists of the input source term of Chalikov and Belevich (1993) and Chalikov (1995) and two dissipation constituents. This is the most widely utilized package in literature.

(2) WAM cycle4 source terms based on wave growth theory of Miles (1957), modified by Janssen (1982), and extended by Abdalla and Bidlot (2002). The default "namelist" parameters are utilized after the modification of Bidlot, Jassen, and Abdallah (hereafter referred to as BJA).

(3) Parameterization with switch ST4 provided by Ardhuin et al. (2010) employs a positive part of the wind input from WAM4 with modified friction velocity u_* to balance saturation-based dissipation. Swell dissipation S_{out} is provided explicitly as part of the wind input source term, indicating that waves may lose energy up in the air. The dissipation term is defined as the sum of the saturation-based term, the cumulative breaking term, and the wave-turbulence interaction term (Ardhuin et al., 2009). The previous ideal setup of Ardhuin et al. (2010) in WWIII version 3.14 is called ACC350, which refers to the authors (Ardhuin, Collart, and Chapron) who developed the S_{out} term.

(4) The Babanin/Young/Donelan/Rogers/Zieger (BYDRZ) scheme implements observation-based physics for deep-water source/sink terms (hereafter referred to as ST6) and includes negative wind input, white capping dissipation, and wave-turbulence interactions (swell dissipation).

Detailed parameterizations of these schemes can be found in the Appendix. In this section, we review the calibration of several models using the packages mentioned.

TC package calibration was carefully performed by Hanson et al. (2009) by using Oceanweather NRAQ+ wind in year 2000 on a 0.5° grid. The performance scores in their work reveal that the capability of WWIII hindcast depends on wave maturity, with swell height being the most significant factor that degrades model performance. This error emanates from winter swell produced in the North Pacific. WAM4 dissipation is a widely utilized parameterization justified by random pulse theory and is successful in the estimation of significant wave height and peak period, including the use of the BJA package (Bidlot et al., 2005). However, these dissipation parameterizations are argued to be inconsistent with the underlying theory and are rather a tuning knob to close the wave energy balance.

For ACC350 and the following ST4 parameterizations, the problem of swell height has been considered in introducing new observation-based nonlinear dissipation (Ardhuin et al., 2010). The dissipation source terms also parameterize wave breaking statistics properties. ACC350, which has been tuned and recorded in WWIII v3.14, exhibits the best performance. After the publication of v4.18, this package updates the swell dissipation part and combines the viscous and turbulent boundary layer expressions. ST4 in this study takes the parameters similar to their TEST451f (see manual), which was used in the study of Saha et al. (2010).

The ST6 package was first described and applied in WAVETIME by Tsagareli et al. (2009) and Babanin et al. (2009) and then later in the SWAN model by Rogers et al. (2012) and in WWIII by Zieger et al. (2011). Two novel features of wind-input source functions are incorporated based on observations of young wave development. The cumulative and threshold behaviors for breaking are also considered. The parameters employed here are similar to those set in the default ST6 switch in WWIII.

With regard to the swell dissipation process, both ST4 and ST6 present explicit parameterizations. ST4 speculates that swell decay could be the result of shear stress modulations caused by swell orbital velocities in the atmosphere (Ardhuin et al., 2009). Perignon et al. (2014) recently examined this mechanism by using a RANS model and presented a new decay rate. However, in ST6, the swell dissipation process is parameterized in terms of the interaction of waves with oceanic turbulence (Babanin and Haus, 2009; Babanin, 2012). Young et al. (2013) showed that formulations of the two are functionally equivalent and that other candidate mechanisms need to be investigated. Nevertheless, the

model performance of Pacific swells differs under overall tuning, as discussed in the following sections.

3 Pacific hindcast experiments

Five experiments were conducted according to the selected source term packages. Table 1 shows the abbreviations and switches opened. EXP2 and EXP3 run with WWIII v3.14. BJA (EXP2) is the default setting when using ST3 and is better than the original WAM4. ACC350 (EXP3) is the first to add the novel swell dissipation term to reduce the wind input. ST4 (EXP4, using TEST451f settings) is based on the improved version established by Ardhuin et al. (2010) and Rascle and Ardhuin (2013), with the wave growth parameter ($_{max}$) set to 1.33 (better than the default of 1.55 when using CCMP wind). ST6 (EXP5) takes the default settings in WWIII.

The model domain is the outer rectangular box in Fig. 1.

Table 1. Five experiments with specific setup

	EXP1	EXP2	EXP3	EXP4	EXP5
Abbreviation	TC	BJA	ACC350	ST4	ST6
Main switch	ST2 STAB2	ST3 STAB3	ST3 STAB3	ST4	ST6
Main parameter settings	Default settings in WWIII v4.18	Table 2.3 in the WWIII v3.14 manual; without "swell dissipation"	Table 2.3 in the WWIII v3.14 manual; with"swell dissipation"open	TEST451f in WWIII v4.18	Default settings in WWIII v4.18

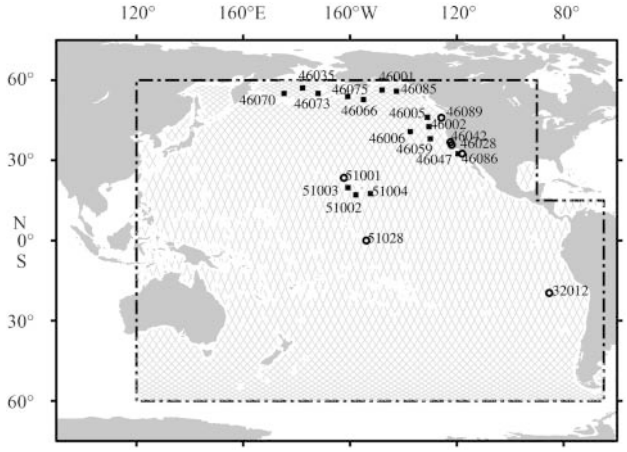

Fig. 1. Model domain (outer rectangular box), JASON-1 H_s selection domain (dash-line polygon), satellite orbits (grey lines), and NDBC buoy data positions (buoys marked "o" have 2D spectra).

Etopo 1' data were utilized to produce 0.5° topography and the sub-grid information file. Twenty-five frequencies were set from 0.04 Hz to 0.4 Hz with an increment factor of 1.1. Thirty-six directions were set with 10° intervals. In most of the area, water depth is larger than 3 000 m. The wind field is 0.25° at 6-hourly interval, which reflects large to mesoscale weather systems. Wind was the only forcing condition, and no nesting or boundary conditions were used. The boundary influence can be omitted because it is far from the area we are interested in. Although the experiments were implemented with two versions of WWIII, the source term schemes exhibit predominant differences; the propagation and nonlinear interaction schemes are consistent. The models were run from initially calm conditions in December 2006 to the end of 2007; only the results of 2007 were retained in the assessment. The following outputs were utilized: the 3-hourly wave field of significant wave height (H_s), mean wave period (T_m), mean wave direction (D), mean wave length (L) and Stokes transport, point output of buoy hourly wave parameters, wave spectrum and source terms, point output of SAR observation time wave parameters, and spectra. According to the different switches and parameter values, the model results of the five experiments were stored separately and post-processed in the same manner to allow for inter-comparison.

3.1 *Validation datasets*

To evaluate the wind forcing and model results, three sources of observation data were acquired as ground truth. The three are JASON-1 satellite altimeter H_s data (distributed by GlobWave at http://globwave.ifremer.fr/products/globwave-satellite-data/altimeter-l2p-data), NDBC buoy meteorological parameters and wave spectra (collected and made available for free by NOAA/NDBC), and ENVISAT satellite advanced synthetic aperture radar (ASAR) wave mode and wave spectra data (http://globwave.ifremer.fr/Products/GlobWave-Satellite-Data/SAR-L2P-data).

A total of 6 014 tracks of JASON-1 H_s data with 720 125 observations were selected from the year 2007; the data cover the entire Pacific Ocean (sample tracks are shown in Fig. 1; observations inside the dash-line polygon are retained). Data within 100 km to the coast were disregarded to avoid landmass contamination. The modeled 3-hourly gridded H_s were interpolated in space and time onto the altimeter tracks. Given that altimeter data can only provide H_s, the historical records of 22 buoys from NDBC were selected to evaluate wind speed, H_s, T_m, and D; part of the buoys' 1D spectra were retained. The 2D wave spectra records of seven buoys can be calculated (with frequency mainly ranging from 0.02 Hz to 0.485 Hz; see Fig. 1 for buoy position). ENVISAT ASAR wave mode data can also provide wave spectra information in the relatively low-frequency bands, that is, swell partitions can be separated to validate model results. A total of 1 720 effective ASAR observations were used in the verification. The model outputs of the corresponding hourly buoy and ASAR data along track parameters are stored. Partitioned wind-sea and swell wave parameters can be obtained by using spectra energy partitioning method (SEP) (Hanson and Phillips, 2001; Hanson and Jensen, 2004; Bi, 2013) and spectra integral method similar to the WW3 model output (see Chapter 2.4 in the WWIII v4.18 manual). After cross calibration, the buoy spectra attributes achieved good quality; for the ASAR observations, the calculated wave length and wave direction were found to be more reliable and accurate than swell height; this finding was also reported in previous literature (Ren et al., 2011).

3.2 *Wind forcing calibration*

Cross-calibrated multi-platform ocean surface wind velocity (CCMP) was utilized as the only forcing field in this study. It was provided by NASA PO.DAAC and distributed by NCAR's CISL Research Data Archive. CCMP is used extensively in wave modeling

(Zhang et al., 2011; Zhang et al., 2013a; Zheng et al., 2013), and its accuracy has been carefully examined in our related work (Bi, 2013). We recall the main procedures and results here. The 2007 10 m surface wind vectors with 6-hour intervals were evaluated against both buoy observations and ENVISAT SAR wind data. A total of 19 096 SAR observations with wind speed of up to 25 m/s provided an *rmse* of 1.89 m/s. To compare the wind directions, the ECMWF model's wind direction data on SAR wind observation time and location were used. The angle bias was only 1.27°. Wind speed differences larger than 5 m/s are more obvious in high latitudes than in tropical oceans because of the intense low-pressure systems and strong storms.

The wind vectors of 21 NDBC buoys in the Pacific Ocean were calibrated separately, except for buoy 32 012 because of the lack of data in 2007. The mean *rmse* is 1.25 m/s, with a mean angle bias 10.4°. Buoy wind bias is almost linear with distance to the coast; observations close to the land or island are less accurate than those far from the coast. The same observation was found in the SAR wind error distributions. The wind speed *rmse* ranges from 0.82 m/s to 2.13 m/s, and the wind direction angle bias ranges from 4.31° to 18.91°. Compared with ECMWF ERA interim data interpolated into buoy positions, the time series of CCMP have more details and follow the variations of hourly buoy wind speed better, regardless of the ones close to the coast or those with less topographic influence. CCMP wind is generally reliable and accurate to use in Pacific Ocean wave simulations.

3.3 *Performance indicators*

As mentioned above, two types of methods were utilized in model verification to facilitate the selection of the model setup and alleviate possible *rmse*-based error analysis shortcomings.

The performance evaluation method proposed by Hanson et al. (2009) calculates the error metrics of integrated and partitioned wave attributes and scores the weighted overall performance. This method significantly reduces the database and makes it easier to obtain a general conclusion. The steps of the method and some of the modified procedures are as follows. First, SEP was used to separate wind wave and swell components. This procedure can be automatically implemented with a Matlab package (Bi, 2013). Given the wind speed, wind direction, and wave 2D spectra, the wave attributes (e.g., H_s, T_m, D, and L) can be calculated through spectra-partition-based integration and stored for the wind sea and the first two energetic swell partitions. Buoy and ASAR wave spectra partition template was utilized to identify the corresponding partitions in the hindcast spectra of the five experiments.

Second, error analysis was conducted to quantify the differences between hindcast and observations. For n values of JASON-1 H_s, buoy measurements or ASAR partition attributes (X_0, which refers to observations), and the corresponding model results (X_m), the following metrics were calculated (Hanson et al., 2009).

Mean bias

$$b = \frac{1}{n}\sum_{i=1}^{n}(X_{i,\mathrm{m}} - X_{i,\mathrm{o}})\,, \tag{2}$$

mean relative bias

$$b_{\mathrm{re}} = \frac{1}{n}\sum_{i=1}^{n}\frac{X_{i,\mathrm{m}} - X_{i,\mathrm{o}}}{X_{i,\mathrm{o}}}\,, \tag{3}$$

root mean sequare error

$$rmse = \sqrt{\frac{\sum_{i=1}^{n}(X_{i,\mathrm{m}} - X_{i,\mathrm{o}})^2}{n}}\,, \tag{4}$$

and scatter index (SI)

$$SI = \frac{\sigma_{\mathrm{d}}}{\overline{X}_{\mathrm{o}}}\,, \tag{5}$$

where the standard deviation of the difference is provided by

$$\sigma_{\mathrm{d}} = \sqrt{\frac{\sum_{i=1}^{n}(X_{i,\mathrm{m}} - X_{i,\mathrm{o}} - b)^2}{n-1}}\,. \tag{6}$$

For wave directions, the metrics used were angular bias

$$b_{\mathrm{a}} = \begin{cases} \arctan\left(\dfrac{S}{C}\right), & S>0, C>0; \\ \arctan\left(\dfrac{S}{C}\right)+\pi, & C<0; \\ \arctan\left(\dfrac{S}{C}\right)+2\pi, & S<0, C>0; \end{cases} \tag{7}$$

in which $S=\sum_{i=1}^{n}\sin(\Delta\theta_i)$, $C=\sum_{i=1}^{n}\cos(\Delta\theta_i)$, and $\Delta\theta_i = |\theta_{\mathrm{m}} - \theta_{\mathrm{o}}|$ (difference between the model result and observation), and (2) circular correlation

$$cor = \frac{\sum_{i=1}^{n}\sin(\theta_i,\mathrm{o}-\overline{\theta}_{\mathrm{o}})\sin(\theta_i,\mathrm{m}-\overline{\theta}_{\mathrm{m}})}{\sqrt{\sum_{i=1}^{n}[\sin(\theta_i,\mathrm{o}-\overline{\theta}_{\mathrm{o}})]^2\sum_{i=1}^{n}[\sin(\theta_i,\mathrm{m}-\overline{\theta}_{\mathrm{m}})]^2}}\,. \tag{8}$$

A set of monthly and yearly error metrics of physical attributes (H_s, T_m, D, and L) of the overall sea wave and partitioned wind sea and swell components are retained.

Lastly, performance indicators for overall skill assessment were generated after normalization of individual metrics. All performance parameters are marked with ^. The *rmse* estimator is represented as $\widehat{rmse}$ and defined like

$$\widehat{rmse} = \frac{rmse}{O_{\mathrm{rms}}}\,, \tag{9}$$

where the root mean square of observation data is

$$O_{\mathrm{rms}} = \sqrt{\sum_{i=1}^{n}X_{i,\mathrm{o}}^2\Big/n}\,, \tag{10}$$

bias performance is

$$\hat{b} = \frac{|b|}{O_{\mathrm{rms}}}\,, \tag{11}$$

scatter index performance is

$$\widehat{SI} = SI\,, \tag{12}$$

angular bias performance is

$$\hat{b}_{\mathrm{a}} = \frac{|b_{\mathrm{a}}|}{180}\,, \tag{13}$$

and circular correlation performance is

$$\widehat{cor} = 1 - cor \,. \tag{14}$$

For non-directional metrics, the performance is

$$P_s = \frac{\widehat{rmse} + \hat{b} + \widehat{SI}}{3} \,. \tag{15}$$

For directional metrics, the performance is

$$P_s = \frac{\hat{b}_a + \widehat{cor}}{2} \,. \tag{16}$$

WhereP_s is slightly different from the estimator $P_{s,H09}$ in the original method of Hanson et al. (2009); non-dimensional P_s ranges from 0 to 1, with 0 indicating perfect performance (P_s=1–$P_{s,H09}$; indicators in Eqs (9) and (11) to (14) are different from their original forms). After calculating individual P_s, the weighted overall performance across all types of observations for each wave attribute is

$$PS = \frac{\sum n_j P_{s,j}}{\sum n_j} \,, \tag{17}$$

where n_j is the number of observations in one subset.

This indicator, PS, combines the generally used error analysis metrics, including *rmse* and *SI*. However, Mentaschi et al. (2013) argued that *rmse*-based validations may result in an underestimated index for simulations in conditions of constant correlation coefficient with negative bias, which does not always signify improved performance. Hence, the indicator proposed by Hanna and Heinold (1985) (HH) was utilized for cross comparison.

$$HH = \sqrt{\frac{\sum_{i=1}^{n}(X_{i,m} - X_{i,o})^2}{\sum_{i=1}^{n} X_{i,m} X_{i,o}}} \,, \tag{18}$$

which ranges from 0 (perfect performance) to 1 (no correlation) and matches PS in performance assessment. In the following analysis, HH is applied to non-directional attributes. Disagreement between PS and HH is rarely observed but would still be recorded and explained if necessary.

4 Result analysis

4.1 *Model performance of overall energy distribution*

The modeled H_s is interpolated into JASON-1 position, and the indicators (PS and HH) are shown in Fig. 2. All experiments exhibited improved performance between 3 m and 9 m, and small and strong waves were less accurate. TC, ST4, and ST6 are generally better than BAJ and ACC350; this result shows the stability of TC and the improvement of the newly implemented packages. ST4 performs well when H_s is smaller than 7 m, and ST6 performs well when waves are higher than 7 m. Both PS and HH show similar trends, indicating the consistency of the analysis. The *rmse* values of the experiments are 0.52, 0.58, 0.58, 0.39, and 0.47 m, revealing that ST4 is generally better than the others. The normalized mean bias of ST6 shows a negative trend when H_s is below 7 m, whereas all other experiments show positive bias when H_s is below 3 m. Compared with that in Rascle and Ardhuin's study (2013), the trend of H_s bias in the current study is similar but has a larger error, indicating that Pacific high waves still requires tuning; nesting would further improve the performance. The *rmse* values (on a monthly basis) in April and September are slightly larger in all experiments, but ST4 and ST6 exhibit much improvement.

The PS and HH of H_s and T_m against buoy time series are shown in Fig. 3. The H_s of the buoys at northeast Pacific reveals that ST4 is generally better than the others, and ST6 exhibits smaller errors in representing waves in the area of Hawaii and buoy 51028. The simulated T_m is the best when TC is used, but the positive bias of T_m exists in all setups mainly because of the swell period bias (to be further discussed in the following section). As for the *D* simulations, only PS was calculated. Although TC appears to be better than the other schemes, the actual PS differences among the schemes are small (approximately 0.05), and the individual statistics of angular bias of *D* are within 10°; that is, all experiments performed well in reflecting wave propagation directions.

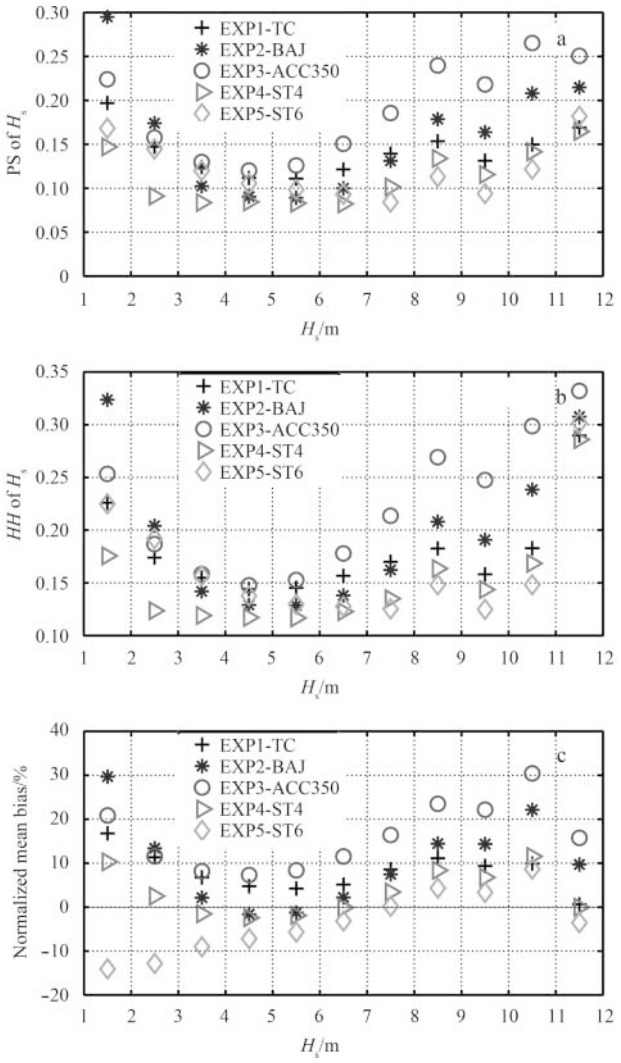

Fig. 2. Performance indicator PS (a) and HH (b) of the modeled H_s against JASON-1 H_s and normalized mean bias as a function of H_s (c).

4.2 *Wave partitions analysis*

As mentioned in the Pacific wave model assessment by Hanson et al. (2009), the parameters obtained from integral properties of the wave spectrum are inadequate to identify model

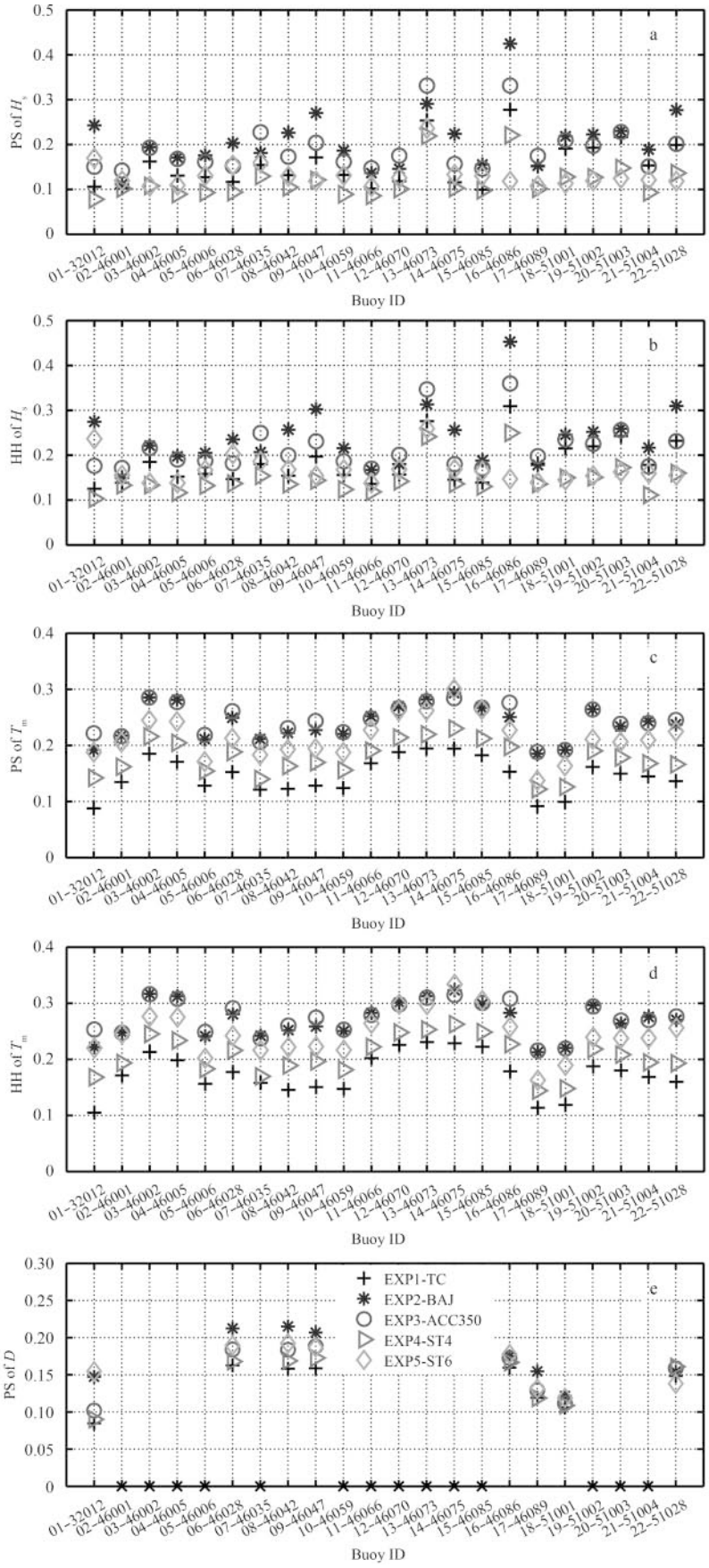

Fig. 3. Performance indicator against buoys of all experiments. a. PS of H_s, b. HH of H_s, c. PS of T_m, d. HH of T_m, and e. PS of D. The buoy IDs are listed at the bottom.

strengths and deficiencies. After SEP, ENVISAT ASAR swell partitions are retained. The measured L is a direct parameter in representing swell, which ranges from approximately 50 m to 500 m. The *rmse* values of the experiments are 45.4, 53.8, 60.3, 49, and 46.6 m. The normalized biases of L are mainly positive in all the experiments, indicating the possible source of wave period bias as reported from the buoy verifications. The swell height is not so accurate according to cross calibration mentioned in Ren et al. (2011) but was still recorded in our analysis for reference. The D of ENVISAT swells are not extremely sensitive to source term changes and the *rmse* values are maintained at about 8°, indicating the capability of all the models to represent remote energy propagation patterns. The PS of swell that consists of L and D is shown in Fig. 6 (in yellow line).

Buoys that have 2D spectra records (circles in Fig. 1) were carefully examined. The wind sea H_s tends to be slightly underestimated in all the experiments, with ST6 having the largest negative bias. However, ST6 performs best in grasping the swell height variation of all buoys. The normalized *rmse* is defined as $rmse_N = \sqrt{\sum_{i=1}^{n}(X_{i,m} - X_{i,o})^2} \Big/ \sum_{i=1}^{n} X_{i,o}^2$ and is shown in Fig. 4. Wind sea H_s (Fig. 4a) and T_m (Fig. 4c) are generally better than those in swell simulation (Figs 4b and d), which was also pointed out by Hanson et al. (2009), using only buoy 51028. These buoys mainly belong to four types of wave systems. The wave roses of wind sea and the first two energetic swell partitions are shown to clarify the mixed situations (Fig. 5). Buoy 46089 (Fig. 5a, Category I) has very strong local wind sea; storm-induced swells are directed mainly to the northeast and southeast together with small successive swells and makes energy distributions complicated and highly nonlinear (observations only in December). All the five schemes produced very close PS of wind sea H_s at this buoy station. Buoys 46028, 46042, and 46086 (Fig. 5b, Category II) are all located in the west coast of North America and Mexico, with similar decaying swells from the westlies and local wind sea in the same directions. However, EXP1 to EXP3 exhibited significant scattering in the simulating swells at these adjacent locations (Fig. 4b). This finding indicates that (1) TC, BJA, and ACC350 are not as stable as ST4 and ST6 in this wave state and (2) ST6 is superior in reducing the swell bias in the coastal oceans but not as accurate as the others in the wind sea H_s simulations (see the larger PS of EXP5 in Fig. 4a). Buoy 51001 in the northwest of Hawaii faces the swells coming from the north and often records long wave trains from the south ocean simultaneously, which are often opposite in directions; meanwhile, local swells are also formed under the easterly wind belts. Buoy 51028 (Fig. 5c, Category III) in the tropical ocean is similar. Local wind sea and following swells propagate to the west together with swells to the north, but swells from the north storms are weaker. Buoy 32012 (Fig. 5d, Category IV) is the only one in the south Pacific recording intense swells from the south ocean storms toward the northeast and also turning winds blowing to the northwest, inducing wind sea and weak following swells (observations only in December). The local wind sea and primary swells are almost equally strong, and the ST6 deficiency in reflecting wind sea energy can be found in the large PS in Fig. 4a.

The improvements of ST4 and ST6 in mixed situations are generally obvious both in wind sea and swell partitions. However, ST6 is inconsistent in reflecting the wind sea H_s variations (especially in Buoy 32012) and introduces errors in the overall performance analysis. The assessment above shows that TC, BJA, and ACC350 are generally not as accurate as ST4 and ST6 in representing mixed wave systems in different areas. The swell energy simulations for the ST6 setup reveal that this setup has the least scatter in all buoys (Fig. 4b), indicating the adaptability of this new scheme. Moreover, T_m swell bias was observed again in accordance with the L analysis made by ASAR observations.

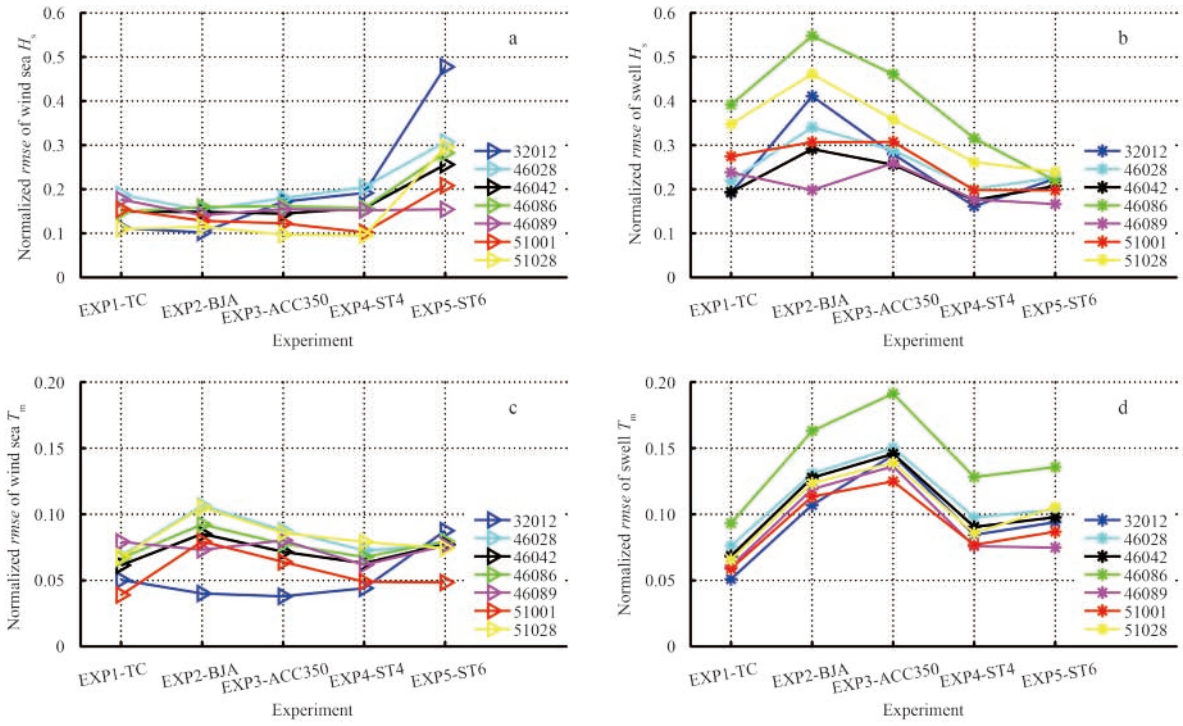

Fig. 4. Normalized *rmse* of wave partitions against seven 2D buoys of all experiments. a. Wind sea H_s, b. swell H_s, c. wind sea T_m, and d. swell T_m. The most energetic swell partition is displayed.

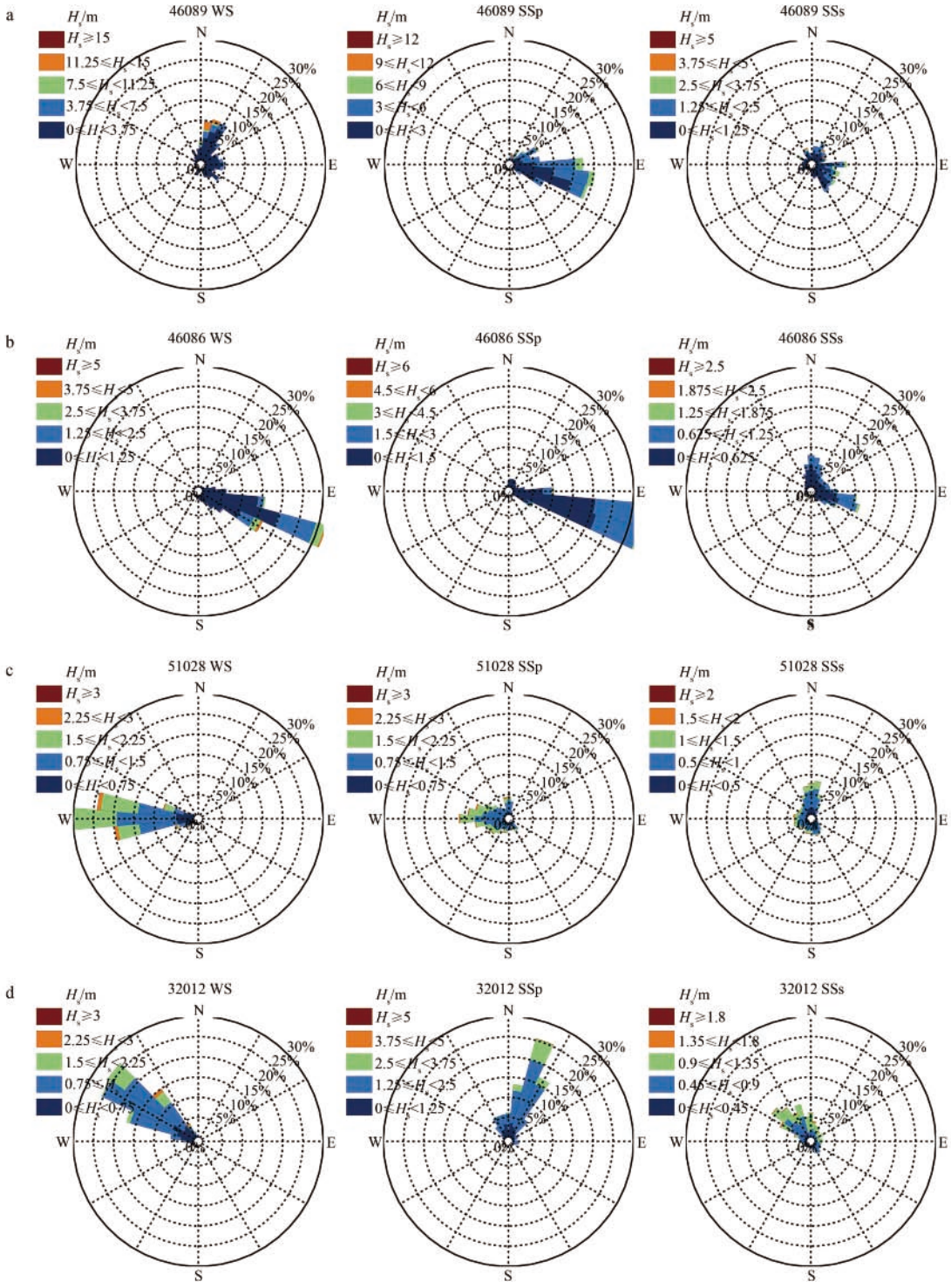

Fig. 5. Wave height rose of Buoys 46089 (a), 46086 (b), 51028 (c), and 32012 (d) representing four types of wave climates. Directions indicate where the waves go. From left to right are wind sea (WS), the most energetic swell (SSp), and secondary swell (SSs) partitions.

4.3 *General performance summary*

The overall PS was calculated according to the detailed verifications against different ground truth data and analysis of wave partitions and is shown in Fig. 6. The PS and HH of ENVISAT ASAR swell parameters are consistent, and the overall PS (in yellow line) only considers swell D and L. Figure 6 also shows the PS of all buoy wind sea (Buoy WS), first energetic swell (Buoy SSp), secondary swell (Buoy SSs), buoy PS of all partitions, PS of JASON-1 H_s (grey dash line), and PS of all the above ground truth datasets (black line). ST6 is generally ideal in terms of reproducing the swell variations but not as accurate as ST4 in wind sea partitioning. The overall PS considering all observations reveals ST4 as the primary choice for the subsequent long-term and background wave hindcasts.

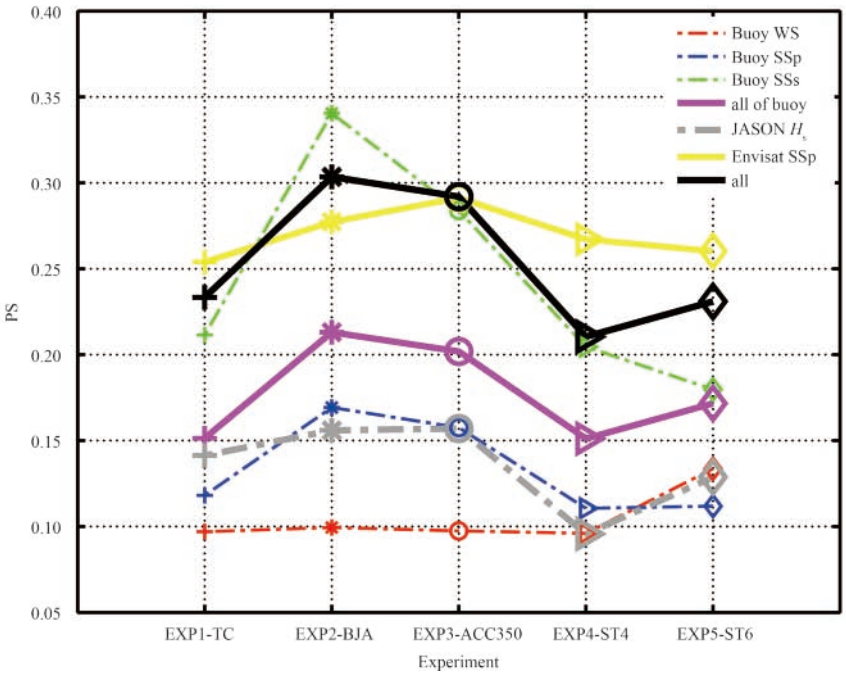

Fig. 6. Performance index PS of all attributes. Buoy wind sea (Buoy WS), first energetic swell (Buoy SSp), secondary swell (Buoy SSs) and buoy PS of all partitions (all buoys) consisting of H_s, T_m, and D. The PS of JASON-1 H_s is in grey dash line. The PS of ENVISAT ASAR using D and L of SSp is in yellow line. The PS of all the above ground truth datasets is denoted by a black line.

5 Wave-induced upper ocean flux and transport

In addition to the assessment for wave climate research, background wave field analysis, and forecast of wave parameters and spectrum, datasets for geophysical applications are needed in wave-current-turbulence interactions (Rascle et al., 2008) and air-sea interactions (Rascle and Ardhuin, 2013). Wave-induced velocity and mass transport in upper ocean dynamics and the contribution of wave effects are usually analyzed by using integrated wave parameters (McWilliams and Restrepo, 1999; Bi et al., 2012; Zhang et al., 2013b; Bi and Wu, 2014). In this study, we further examined the performance of several selected schemes in modeling wave-induced flux and transport.

5.1 *Wave-related momentum flux*

Wave-induced stress is believed to change the lower boundary layer of the atmosphere. Upward momentum flux has been observed (Harris, 1966; Grachev and Fairall, 2001; Hanley and Belcher, 2008) and is found to be prevalent in swell-dominated situations (Hanley et al., 2010). Wave breaking, together with other physical processes, dissipates most of the wave energy into the ocean. Surface waves act as an interface and passage in ocean flux and energy transfer.

Considering the surface waves, the steady wave-modified Ekman horizontal currents satisfy the following equation for a deep, vertically homogeneous ocean of infinite lateral extent.

$$\rho\vec{f}\times(\vec{u}+\vec{u}_S)=\frac{\partial\vec{\tau}}{\partial z}-T_{ds}\,, \tag{19}$$

$$\vec{\tau}=\vec{\tau}_a-\vec{\tau}_{in},\ z=0\,, \tag{20}$$

where $\vec{f}$ is the planetary vorticity, $\vec{u}$ is the mean current, $\vec{u}_S$ is Stokes drift, and $\vec{\tau}$ is turbulent stress. On the sea surface, wind stress $\vec{\tau}_a=\rho_a\vec{u}_*|u_*|$, where $\vec{u}_*$ is the air side friction velocity. For wave-induced stress on the surface,

$$\tau_{in}=\rho_w\iint\omega k\,(\cos\theta,\sin\theta)\,S_{in}\,(k,\theta)\,\mathrm{d}k\mathrm{d}\theta\,, \tag{21}$$

indicating that the flux directly transferred to the waves. For wave-induced momentum transfer from waves to ocean because of energy dissipation,

$$T_{ds}\,(z)=2\iint\omega k e^{2kz}\,(\cos\theta,\sin\theta)\,S_{ds}\,(k,\theta)\,\mathrm{d}k\mathrm{d}\theta\,, \tag{22}$$

which is often considered in wave–current interactions (Jenkins, 1986, 1987; Tang et al., 2007; Song, 2009).

The above two terms are mainly based on wave input and dissipation source terms. This condition means that different choices of source term packages result in different wave influences. For brevity and clarity, we adopted depth integration in Eq. (19) and compared the source terms from the perspective of "transport".

The depth-integration of the wave modified motion in Eq. (19) results in the transport equation

$$T+T_S=-\frac{\hat{z}\times\vec{\tau}_a}{f\rho}-\left(-\frac{\hat{z}\times\vec{\tau}_{in}}{f\rho}-\hat{z}\times\int T_{ds}\mathrm{d}z\right)\,, \tag{23}$$

where $T=\int_{-\infty}^{0}\vec{u}\mathrm{d}z$ and $T_S=\int_{-\infty}^{0}\vec{u}_S\mathrm{d}z$. T_s is the so-called wave-induced Stokes transport across the unit length perpendicular to the wave propagation direction. $W_{in}=-\frac{\hat{z}\times\vec{\tau}_{in}}{f\rho}=\left(\frac{\tau_{in,y}}{f\rho},-\frac{\tau_{in,x}}{f\rho}\right)$ is the wave-stress-induced transport reduction, $W_{dis}=-\hat{z}\times\int T_{ds}\mathrm{d}z=\left(\int T_{ds,y}\mathrm{d}z,-\int T_{ds,x}\mathrm{d}z\right)$ is the wave-dissipation-induced transport increase, and $W_a=-\frac{\hat{z}\times\vec{\tau}_a}{f\rho}=\left(\frac{\tau_{a,y}}{f\rho},-\frac{\tau_{a,x}}{f\rho}\right)$ is the traditional ageostrophic wind-induced transport. The equations above take the following form.

$$T_x+T_{S,x}=\frac{\tau_{a,y}}{f\rho}-\left(\frac{\tau_{in,y}}{f\rho}+\int T_{ds,y}\mathrm{d}z\right)=W_{a,x}-(W_{in,x}+W_{dis,x}), \quad (24)$$

$$T_y+T_{S,y}=-\frac{\tau_{a,x}}{f\rho}-\left(-\frac{\tau_{in,x}}{f\rho}-\int T_{ds,x}\mathrm{d}z\right)=W_{a,y}-(W_{in,y}+W_{dis,y}). \quad (25)$$

Different source term packages result in different wave flux influences. The three terms at the right side of Eq. (23) were examined based on the wave spectrum of the buoys. Figure 7 shows wave-stress-induced transport W_{in} and total wave-induced transport $W_{in}+W_{dis}$ versus traditional wind-induced ageostrophic transport W_a at Buoy 51001. The transport is based on a steady state assumption, and the Ekman transport is mainly less than 10% of the total upper ocean transport, including geostrophic currents measured with the Sverdrup relation (Bi and Wu, 2014). The wave-induced transport difference caused by source term choices is the main focus in this section, and the wave-induced transport portion in the total ocean transport is beyond the scope of this study.

Here, W_a depends on u_* of different source term packages. Buoy 51001 is in the northwest of Hawaii Islands, and both local winds and remote swells affect the wave climate in the entire year. In Fig. 7, only the transport in the latitudinal direction is shown; longitudinal transport has a similar pattern. The best three schemes, i.e., TC, ST4 and ST6, are compared; BJA is retained for comparison with ST4 to determine the effect of the added swell dissipation term. Figure 7a shows $W_{in,x}$ versus $W_{a,x}$. $W_{in,x}$ is smaller than $W_{a,x}$ as expected. The $W_{in,x}$ of ST6 in a fraction of $W_{a,x}$ is smaller than that in the other three experiments; however, the magnitude of total wave-induced transport $W_{in,x}+W_{dis,x}$ among the schemes is very close (Fig. 7b). In other words, the compensation of wave-dissipation induced transport increase is generally in accordance with the wave-stress induced transport reduction. However, differences can still be found. If the wave effect is considered in upper layer transport evaluation, using ST6 would result in the least transport reduction. Meanwhile, wave-induced transport reduction and increase are not totally in balance, i.e., the magnitude of $W_{in,x}+W_{dis,x}$ is not always close to zero. This condition is more obvious when local wind $W_{a,x}$ is stronger, which induces larger deviations from zero (Fig. 7b). This effect is more obvious in the ST4 and ST6 packages. ST4 shares the positive part of the input source term with BJA and adds a negative S_{out} according to swell dissipation. This can be seen in the decrease of $W_{in,x}$ in ST4 compared with BJA. The annual mean $W_{in,x}/W_{a,x}$ and $W_{in,x}+W_{dis,x}/W_{a,x}$ of the four experiments at buoy 51001 position are shown in Table 2. Considering the all-year data, ST6 wave-induced influence is the least obvious among those of all the four source term packages. Statistics at the other buoy locations provide similar results. In other words, for stronger waves, the dissipation of ST6 is weaker than that of the other schemes. If the wave-induced effect in the upper ocean or atmospheric boundary layer is considered in following research (e.g., air–wave–current model coupling), the choice of wave model source term packages should be made carefully.

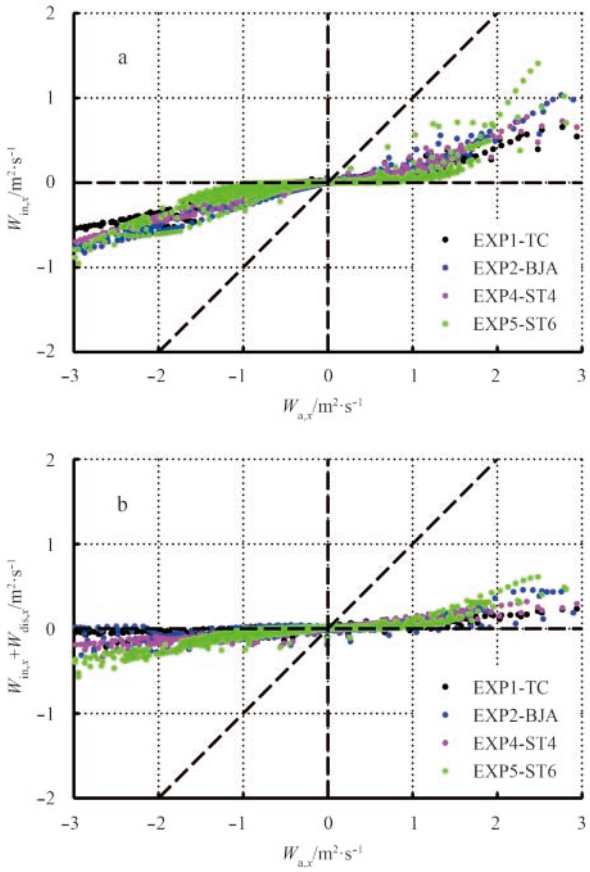

Fig. 7. Wind and wave-induced transport in *X* direction at Buoy 51001 location. a. $W_{in,x}$ against $W_{a,x}$ and b. $W_{in,x}+W_{dis,x}$ against $W_{a,x}$.

Table 2. Wave-induced transport fraction in wind-driven ageostrophic transport

Buoy 51001	TC	BJA	ST4	ST6
Annual mean $W_{in,x}/W_{a,x}$	0.085	0.106	0.060	0.032
Annual mean $W_{in,x}+W_{dis,x}/W_{a,x}$	0.036	0.044	0.050	0.023

5.2 *Stokes transport*

The Stokes transport fraction in wind-driven Ekman transport can reach 40% in the westerly wind regimes between about 40° and 60° (McWilliams and Restrepo, 1999). In the equatorial area, remote-swell-induced cross-equator transport persists through most of the year (Bi et al., 2012). The wave-induced divergences and convergences produce vertical velocities comparable to mean Ekman pumping/suction in the open ocean in high wind regimes (Bi and Wu, 2014) and over the western boundary currents (Tamura et al., 2012). The Stokes transport distribution is directly compared in this section. Using the 1D buoy spectrum and the corresponding WWIII result yields

$$U_s=2\int_{-\infty}^{0}\int_{0}^{\infty}\omega k\mathrm{e}^{2kz}E(f)\,\mathrm{d}f\mathrm{d}z\,, \quad (26)$$

in which the integration was obtained from 0 to the resolved max frequency f_{max}, and from –500 m to 0 (surface) in depth. Buoy data were first interpolated into the WWIII frequency range before integration. This simplification of U_s from using 2D spectra (similar to Kenyon (1969) and Tang et al. (2007)) to 1D spectra is based on the splitting of the wave spectrum into frequency-dependent and directional-distribution parts. This will introduce directional spread loss (Webb and Fox-Kemper, 2011). Equation (26) may overestimate the magnitude of Stokes transport. However, most of the buoys only record non-directional spectrum, and the ASAR 2D spectrum is unreliable in short wave

range (Ren et al., 2011). To reduce the deviation, a roughly global mean spread loss of 75% is multiplied by the calculated U_s (Webb and Fox-Kemper, 2011), which would not affect the assessment. In another word, performance is only determined by how well the model simulates the wave spectrum and wave parameters.

The weighted mean PS of all buoys is 0.26, 0.19, and 0.25 for TC, ST4, and ST6 experiments, respectively. Figure 8 shows the normalized mean bias of each buoy in all three experiments, which indicates the positive bias of TC and negative bias of ST6 at most locations. U_s is proportional to ω^3, which means shorter waves produce larger transport; meanwhile, the depth dependence of e^{2kz} causes longer waves to penetrate deeper into the ocean. The underestimation of ST6 in wind-sea components partly results in the negative bias in U_s, whereas the overall positive bias in H_s of TC gives a clue for its overestimation in U_s.

The yearly mean U_s distributions of TC, ST4, and ST6 (Fig. 9) show similar patterns: the zonal structures are in accordance with wind bands, and existence of obvious swell dominance at about 30°N, 30°S in the eastern part of the Pacific Ocean. U_s between 40°S and 60°S is larger than 0.6 $m^2 \cdot s^{-1}$; it is almost 40% smaller than that calculated by wave parameters under monochromatic wave assumption (Fig. 2 in the paper of Bi et al. (2012)). $U_{s,TC}$ is generally larger than $U_{s,ST4}$, especially in subtropical areas, and the largest normalized difference $(U_{s,TC}-U_{s,ST4})/U_{s,ST4}$ occurs at the middle of tropical oceans by up to 70% (Fig. 10a). $U_{s,TC}$ is smaller than $U_{s,ST4}$ along 30°N to the north of the Aleutian Islands and at the swell convergence zone to the west of Mexico. By contrast, $U_{s,ST6}$ is generally smaller than

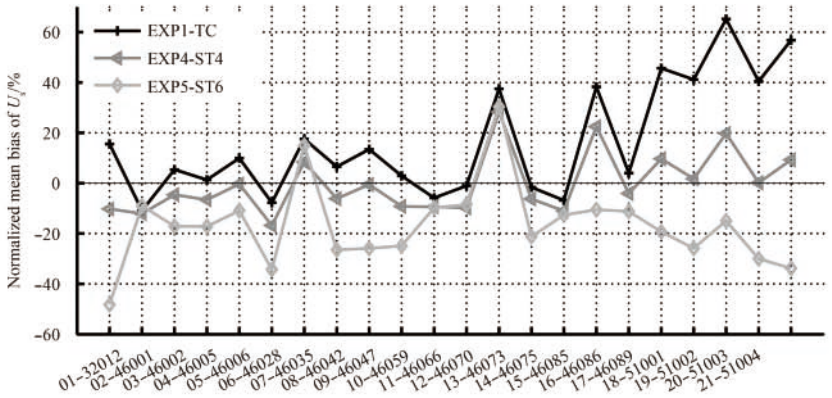

Fig. 8. Normalized mean bias of WWIII Stokes transport against calculated buoy transports.

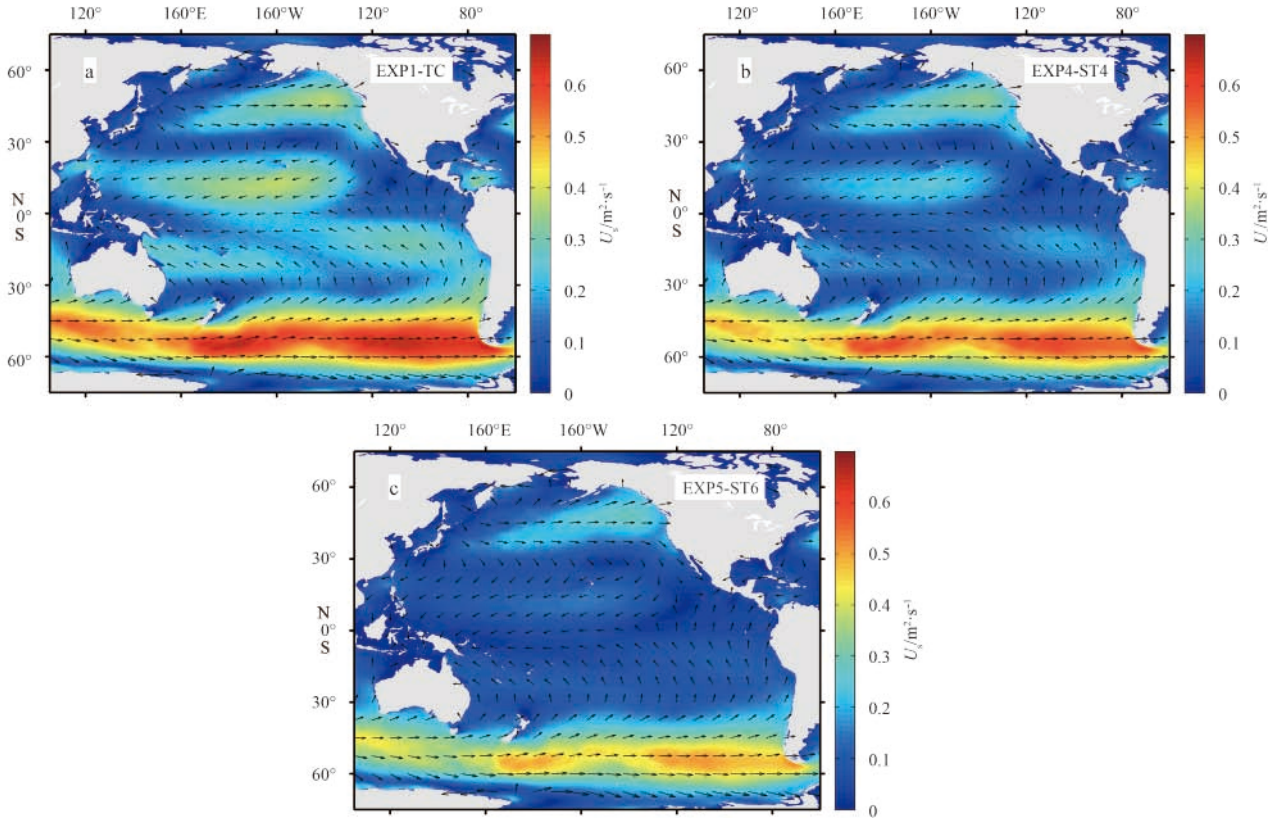

Fig. 9. Annual mean Stokes transport of TC (a), ST4 (b), and ST6 (c) experiments. The shadings denote the magnitude in $m^2 \cdot s^{-1}$, and the arrows indicate the transport direction.

$U_{s,ST4}$, and the largest normalized difference $(U_{s,ST6}-U_{s,ST4})/U_{s,ST4}$ is approximately –60% (Fig. 10b). The disagreements among the three experiments between 30°N and 30°S (especially along the equator) are much larger than at higher latitudes. This area is also where longitudinal U_s dominates most of the year (Bi et al., 2012), indicating strong swell penetration. In addition, the sea state between 30°N and 30°S in much more complicated, with local trade-wind-induced strong eastward waves and swells radiating out of low pressure storms. More than three energetic partitions with different directions can always be found in the local spectrum. Hence, the bias in mixed sea state is still the main source of model uncertainties.

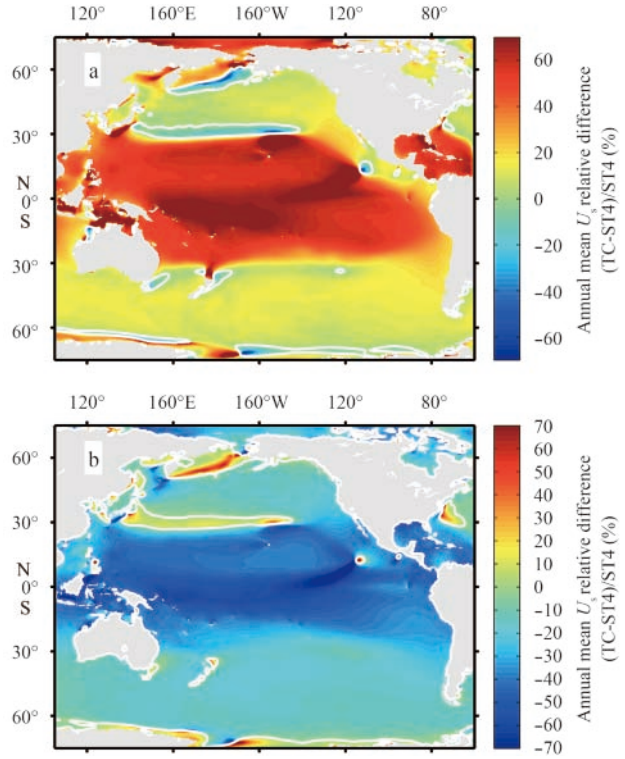

Fig. 10. Stokes transport normalized difference among different packages. The shadings are the normalized difference in percentage, and the contours in white are zero. a. $(U_{s,TC}-U_{s,ST4})/U_{s,ST4}$ and b. $(U_{s,ST6}-U_{s,ST4})/U_{s,ST4}$.

6 Discussion and conclusions

We conducted WWIII experiments on Pacific wave hindcast by using five representative source/sink term packages. Extensive observations, including those for buoy spectra, altimeter H_s, and ASAR swells, were used as ground truth to verify the model simulations. The results were utilized to identify the ideal setup for Pacific wave climate hindcast and other research related to wave–current interactions. The application of the modified performance score method and HH method largely reduces variable numbers. They also facilitate the assessment of model improvements and deficiencies from integrated parameters (H_s, T_m, D) to maturity-related wave systems and partitions (wind sea and swells). The two indexes in the performance analysis, PS and HH, yielded consistent conclusions. For all schemes with different physical and empirical parameters and tunings, wind wave energy is generally better reproduced than swell partitions. Implementing swell dissipation parameterizations, ST4 and ST6 (although based on different physics), improved the performance in low latitude oceans where swell influences are more obvious. D and T_m are more accurate than H_s in all experiments.

TC, ST4, and ST6 were employed to evaluate momentum flux and transport. The model results were compared with buoy spectra integral, in wave-induced transport reduction and increase, and Stokes transport. Total wave stress- and dissipation-induced transport are small compared with Stokes transport but influence the coupling between air-wave-current interactions when selecting different schemes. ST4 is generally better in calculating Stokes transport based on 1D spectra, and TC's overestimation and ST6's underestimation are most obvious in tropical and subtropical oceans where remote swell energy persists. With more physical processes implemented in the model, especially in the dissipation terms, the only dependency of empirical tuning is reduced. As a result of the above analysis, ST4 was selected to perform the following wave climate hindcast, supply background parameters for typhoon wave research in South China Sea, and assist in swell type analysis in the adjacent China Sea.

Acknowledgements

The authors are grateful to all those who provided wind and wave observation data, including NDBC (National Data Buoy Center), the GlobWave Project founded by ESA (The European Space Agency) and CNES (the Centre National d'Etudes Spatiales), and RDA NCAR (Research Data Archive, National Center for Atmospheric Research).

References

Abdalla S, Bidlot J R. 2002. Wind gustiness and air density effects and other key changes to wave model in CY25R1. Rep, Research Department, ECMWF, Reading, UK

Ardhuin F, Chapron B, Collard F. 2009. Observation of swell dissipation across oceans. Geophysical Research Letters, 36(6): doi: 10.1029/2008GL037030

Ardhuin F, Jenkins A D. 2006. On the interaction of surface waves and upper ocean turbulence. Journal of Physical Oceanography, 36(3): 551–557

Ardhuin F, Rogers E, Babanin A V, et al. 2010. Semiempirical dissipation source functions for ocean waves. Part I: Definition, calibration, and validation. Journal of Physical Oceanography, 40(9): 1917–1941

Babanin A. 2011. Breaking and Dissipation of Ocean Surface Waves. Cambridge: Cambridge University Press, 480

Babanin A V. 2012. Swell attenuation due to wave-induced turbulence. Proceedings of the 31st International Conference on Ocean, Offshore and Artic Engineering (OMAE2012), 439–443

Babanin A V, Haus B K. 2009. On the existence of water turbulence induced by nonbreaking surface waves. Journal of Physical Oceanography, 39(10): 2675–2679

Babanin A V, Tsagareli K N, Young I R, et al. 2009. Numerical investigation of spectral evolution of wind waves. Part II: Dissipation term and evolution tests. Journal of Physical Oceanography, 40(4): 667–683

Bi Fan. 2013. On the wave-induced effect to circulation transport and the characteristics of swell propagation and dissipation (in Chinese)[dissertation]. Qingdao: Ocean University of China, 119

Bi Fan, Wu Kejian. 2014. Wave effect on the ocean circulations through mass transport and wave-induced pumping. Journal of Ocean University of China, 13(2): 175–182

Bi Fan, Wu Kejian, Zhang Yuming. 2012. The effect of Stokes drift on Ekman transport in the open sea. Acta Oceanologica Sinica, 31(6): 12–18

Bidlot J R, Abdalla S, Janssen P. 2005. A revised formulation for ocean wave dissipation in CY25R1. in Tech Rep Memorandum R60. 9/JB/0516. Research Department, ECMWF, Reading, UK

Chalikov D. 1995. The parameterization of the wave boundary layer.

Journal of Physical Oceanography, 25(6): 1333–1349
Chalikov D V, Belevich M Y. 1993. One-dimensional theory of the wave boundary layer. Boundary-Layer Meteorology, 63(1–2): 65–96
Dodet G, Bertin X, Taborda R. 2010. Wave climate variability in the North-East Atlantic Ocean over the last six decades. Ocean Modelling, 31(3–4): 120–131
Fan Y, Lin S-J, Held I M, et al. 2012. Global ocean surface wave simulation using a coupled atmosphere–wave model. Journal of Climate, 25(18): 6233–6252
Grachev A A, Fairall C W. 2001. Upward momentum transfer in the marine boundary layer. Journal of Physical Oceanography, 31(7): 1698–1711
Hanley K E, Belcher S E. 2008. Wave-driven wind jets in the marine atmospheric boundary layer. Journal of the Atmospheric Sciences, 65(8): 2646–2660
Hanley K E, Belcher S E, Sullivan P P. 2010. A global climatology of wind–wave interaction. Journal of Physical Oceanography, 40(6): 1263–1282
Hanna S, Heinold D W. 1985. Development and Application of A Simple Method for Evaluating Air Quality Models. Washington DC: American Petroleum Institute
Hanson J L, Jensen R E. 2004. Wave system diagnostics for numerical wave models. In: Proceedings of the 8th International Workshop on Wave Hindcasting and Forecasting. Oahu, Hawaii
Hanson J L, Phillips O M. 2001. Automated analysis of ocean surface directional wave spectra. Journal of Atmospheric and Oceanic Technology, 18(2): 277–293
Hanson J L, Tracy B A, Tolman H L, et al. 2009. Pacific hindcast performance of three numerical wave models. Journal of Atmospheric and Oceanic Technology, 26(8): 1614–1633
Janssen P A E M. 1982. Quasilinear approximation for the spectrum of wind-generated water waves. Journal of Fluid Mechanics, 117: 493–506
Jenkins A D. 1986. A theory for steady and variable wind-and wave-induced currents. Journal of Physical Oceanography, 16(8): 1370–1377
Jenkins A D. 1987. Wind and wave induced currents in a rotating sea with depth-varying eddy viscosity. Journal of Physical Oceanography, 17(7): 938–951
Jiang L F, Zhang Z X, Qi Y Q. 2010. Simulations of SWAN and WAVEWATCH III in northern south China sea. In: Proceedings of the Twentieth (2010) International Offshore and Polar Engineering Conference. Beijing, China: ISOPE, 213–220
Kalantzi G D, Gommenginger C, Srokosz M. 2009. Assessing the performance of the dissipation parameterizations in WAVEWATCH III using collocated altimetry data. Journal of Physical Oceanography, 39(11): 2800–2819
Kenyon K E. 1969. Stokes drift for random gravity waves. Journal of Geophysical Research, 74(28): 6991–6994
Lee Harris D. 1966. The wave-driven wind. Journal of the Atmospheric Sciences, 23(6): 688–693
McWilliams J C, Restrepo J M. 1999. The wave-driven ocean circulation. Journal of Physical Oceanography, 29(10): 2523–2540
Mentaschi L, Besio G, Cassola F, et al. 2013. Problems in RMSE-based wave model validations. Ocean Modelling, 72: 53–58
Miles J W. 1957. On the generation of surface waves by shear flows. Journal of Fluid Mechanics, 3(2): 185–204
Ortiz-Royero J C, Mercado-Irizarry A. 2008. An intercomparison of SWAN and WAVEWATCH III models with data from NDBC-NOAA buoys at oceanic scales. Coastal Engineering Journal, 50(1): 47–73
Padilla-Hernández R, Perrie W, Toulany B, et al. 2004. Intercomparison of modern operational wave models. In: Proceedings of the Eigth International Workshop on Wave Hindcasting and Forecasting. North Shore, Oahu, Hawaii
Perignon Y, Ardhuin F, Cathelain M, et al. 2014. Swell dissipation by induced atmospheric shear stress. Journal of Geophysical Research: Oceans, 119(10): 6622–6630
Rascle N, Ardhuin F. 2013. A global wave parameter database for geophysical applications. Part 2: Model validation with improved source term parameterization. Ocean Modelling, 70: 174–188
Rascle N, Ardhuin F, Queffeulou P, et al. 2008. A global wave parameter database for geophysical applications. Part 1: Wave-current-turbulence interaction parameters for the open ocean based on traditional parameterizations. Ocean Modelling, 25(3–4): 154–171
Ren Qifeng, Zhang Jie, Meng Junmin, et al. 2011. Comparison and analysis of Envisat ASAR ocean wave spectra with buoy data in the northern Pacific Ocean. Chinese Journal of Oceanology and Limnology, 29(1): 10–17
Rogers W E, Babanin A V, Wang D W. 2012. Observation-consistent input and whitecapping dissipation in a model for wind-generated surface waves: Description and simple calculations. Journal of Atmospheric and Oceanic Technology, 29(9): 1329–1346
Saha S, Moorthi S, Pan Hualu, et al. 2010. The NCEP climate forecast system reanalysis. Bulletin of the American Meteorological Society, 91(8): 1015–1057
Song Jinbao. 2009. The effects of random surface waves on the steady Ekman current solutions. Deep-Sea Research Part I: Oceanographic Research Papers, 56(5): 659–671
Tamura H, Miyazawa Y, Oey L-Y. 2012. The Stokes drift and wave induced-mass flux in the North Pacific. Journal of Geophysical Research: Oceans, 117(C8): C08021
Tang C L, Perrie W, Jenkins A D, et al. 2007. Observation and modeling of surface currents on the Grand Banks: A study of the wave effects on surface currents. Journal of Geophysical Research, 112(C10): C10025
Teixeira M A C, Belcher S E. 2002. On the distortion of turbulence by a progressive surface wave. Journal of Fluid Mechanics, 458: 229–267
Tsagareli K N, Babanin A V, Walker D J, et al. 2009. Numerical investigation of spectral evolution of wind waves. Part I: Wind-input source function. Journal of Physical Oceanography, 40(4): 656–666
Webb A, Fox-Kemper B. 2011. Wave spectral moments and Stokes drift estimation. Ocean Modelling, 40(3–4): 273–288
Young I R, Babanin A V, Zieger S. 2013. The decay rate of ocean swell observed by altimeter. Journal of Physical Oceanography, 43(11): 2322–333
Zhang Peng, Chen Xiaoling, Lu Jianzhong, et al. 2011. Research on wave simulation of Bohai Sea based on the CCMP remotely sensed sea winds. Marine Science Bulletin (in Chinese), 30(3): 266–271
Zhang Hongsheng, Gu Junbo, Wang Hailong, et al. 2013a. Simulating wind wave field near the Pearl River Estuary with SWAN nested in WAVEWATCH. Journal of Tropical Oceanography, 32(1): 8–17
Zhang Yuming, Wu Kejian, Zhang Xiaoshuang, et al. 2013b. Improving the estimate of wind energy input into the Ekman layer within the Antarctic Circumpolar Current. Acta Oceanologica Sinica, 32(3): 19–27
Zheng Chongwei, Pan Jing, Li Jiaxun. 2013. Assessing the China Sea wind energy and wave energy resources from 1988 to 2009. Ocean Engineering, 65: 39–48
Zieger S, Babanin A V, Rogers E, et al. 2011. Observation-based dissipation and input terms for a WAVEWATCH III: implementation and simple simulations. In: Proceedings of the 12th Int Workshop on Wave Hindcasting and Forecasting and 3rd Coastal Hazards Symposium. Kohala Coast, Hawaii

Appendix: Parameterizations of the selected source/sink term packages

A1 TC package

The input source term reads

$$S_{\text{in}} = \sigma\beta N(k,\theta), \tag{A1}$$

where β is a non-dimensional wind–wave interaction parameter whose value depends on the non-dimensional frequency and drag coefficient at a height equal to the "apparent" wave length.

The dissipation source term consists of two constituents. The (dominant) low-frequency constituent is based on an analogy with energy dissipation induced by turbulence, i.e.,

$$S_{\text{ds,l}}(k,\theta) = -2u_* hk^2 \phi N(k,\theta). \tag{A2}$$

$$h = 4\left[\int_0^{2\pi}\int_{f_h}^{\infty} F(f,\theta)\mathrm{d}f\,\mathrm{d}\theta\right]^{1/2}, \tag{A3}$$

$$\phi = b_0 + b_1\tilde{f}_{p,i} + b_2\tilde{f}_{p,i}^{-b_3}, \tag{A4}$$

where h is a mixing scale determined from the high-frequency content of the wave field and ϕ is an empirical function accounting for the development stage of the wave field. The empirical high-frequency dissipation is defined as

$$S_{\text{ds,h}}(k,\theta) = -a_0\left(\frac{u_*}{g}\right)^2 f^3 \alpha_{\text{n}}^B N(k,\theta), \tag{A5}$$

$$B = a_1\left(\frac{fu_*}{g}\right)^{-a_2}, \tag{A6}$$

$$\alpha_{\text{n}} = \frac{\sigma^6}{c_g g^2 \alpha_r} N(k,\theta), \tag{A7}$$

where α_{n} is Phillips' non-dimensional high-frequency energy level normalized with α_r. The two constituents of the dissipation source term are combined by using a simple linear combination defined by frequencies f_1 and f_2.

$$S_{\text{ds}}(k,\theta) = AS_{\text{ds,l}} + (1-A)S_{\text{ds,h}}, \tag{A8}$$

$$A = \begin{cases} 1 & \text{for} \quad f < f_1, \\ \dfrac{f-f_2}{f_1-f_2} & \text{for} \quad f_1 \leqslant f < f_2, \\ 0 & \text{for} \quad f_2 \leqslant f. \end{cases} \tag{A9}$$

A2 WAM4 package

The wind–wave interaction source terms of WAM4 are based on wave growth theory proposed by Miles (1957) and modified by Janssen (1982). The source term reads

$$S_{\text{in}}(k,\theta) = \frac{\rho_{\text{a}}}{\rho_{\text{w}}}\frac{\beta_{\max}}{\kappa^2} e^Z Z^4 \left(\frac{u_*}{C}\right)\cos^{p_{\text{in}}}(\theta-\theta_u)\sigma N(k,\theta) + S_{\text{out}}(k,\theta), \tag{A10}$$

where ρ_{a} and ρ_{w} are the air and water densities, $\beta_{\max}$ is a non-dimensional growth parameter, k is von Karman's constant, and p_{in} is a constant that controls the directional distribution. Z=log(kz_1)+κ/[cos(θ–θ_u)(u_*/C+z_α)], and z_α is a wave age tuning parameter. Roughness z_1 is modified by wave-supported stress τ_{w} and is defined as

$$U_{10} = \frac{u_*}{\kappa}\log\left(\frac{z_u}{z_1}\right), \tag{A11}$$

$$z_1 = \alpha_0\frac{\tau}{\sqrt{1-\tau_w/\tau}}, \tag{A12}$$

where τ=u_*^2. τ_w is calculated by the resolved part of the spectrum and a f^{-X} (here, X=5) tail.

A linear damping of swells was introduced but not activated in the default BJA parameterization, namely, S_{out} was set to 0; hence, we do not discuss this part. The generic form of the WAM4 dissipation term is

$$S_{\text{ds}}(k,\theta)^{\text{WAM}} = C_{\text{ds}}\bar{\alpha}^2\bar{\sigma}\left[\delta_1\frac{k}{\bar{k}} + \delta_2\left(\frac{k}{\bar{k}}\right)^2\right]N(k,\theta), \tag{A13}$$

where C_{ds} is a non-dimensional constant and δ_1 and δ_2 are weight parameters. $\bar{k} = \left[\dfrac{\int k^p N(k,\theta)\mathrm{d}\theta}{\int N(k,\theta)\mathrm{d}\theta}\right]^{1/p}$ and $\bar{\sigma} = \left[\dfrac{\int \sigma^p N(k,\theta)\mathrm{d}\theta}{\int N(k,\theta)\mathrm{d}\theta}\right]^{1/p}$, with p being a constant.

A3 ST4 package

In the ST4 package, the linear part of the WAM4 wind input is taken, with an ad hoc reduction of u_* to balance the saturation-based dissipation.

The swell dissipation parameterization of Ardhuin et al. (2009) is different from that of WAM4 and is given by a weighted combination of viscous boundary layer value

$$S_{\text{out,vis}}(k,\theta) = -s_5\frac{\rho_{\text{a}}}{\rho_{\text{w}}}\left\{2k\sqrt{2\nu_{\text{a}}\sigma}\right\}N(k,\theta), \tag{A14}$$

with the turbulent boundary layer expression

$$S_{\text{out,tur}}(k,\theta) = -\frac{\rho_{\text{a}}}{\rho_{\text{w}}}\left\{16 f_e\sigma^2 u_{\text{orb,s}}/g\right\}N(k,\theta). \tag{A15}$$

The full term reads

$$S_{\text{out}}(k,\theta) = r_{\text{vis}}S_{\text{out,vis}}(k,\theta) + r_{\text{tur}}S_{\text{out,tur}}(k,\theta). \tag{A16}$$

The air-sea boundary layer's significant Reynolds number is defined as Re=$2u_{\text{orb,s}}H_{\text{s}}/\upsilon_{\text{a}}$, with threshold Re_c. The two weights are defined to allow for a smooth swell dissipation function around the threshold for transition (Rascle and Ardhuin, 2013).

The dissipation term is defined as the sum of the saturation-based term, the cumulative breaking term, and the wave-turbulence interaction term. The saturation-based term combines an isotropic part and a direction-dependent part. The cumulative breaking term $S_{\text{bk,cu}}$ represents the smoothing of the surface by large breakers that wipe out small waves. The wave-turbulence interaction term $S_{\text{ds}}^{\text{turb}}$ takes the form of that in the studies of Teixeira and Belcher (2002) and Ardhuin and Jenkins (2006). These three parts are all linear to the action spectrum $N(k,\theta)$.

A4 ST6 package

The BYDRZ version deep-water source/sink terms' improvement includes wind input source and sink terms caused by a negative wind input, white capping dissipation, and wave-turbulence interactions (swell dissipation). The wind input and white-capping dissipation source terms are based on measurements taken at Lake George, Australia; those of wave-turbulence dissipation are based on laboratory experiments and field observations of swell decay, and those of the negative input are based on

laboratory testing. A constraint is imposed on the total wind energy input through wind stress.

The input source term implements new features, namely, (1) full air-flow separation that leads to a relative reduction in wind input for conditions of strong winds/steep waves and (2) dependence of the wave growth rate on wave steepness, which signifies the nonlinear behavior of the wind-input source function. Following Rogers et al. (2012), this source term is

$$S_{\mathrm{in}} = \frac{\rho_{\mathrm{a}}}{\rho_{\mathrm{w}}} \sigma\gamma\left(k,\theta\right) N\left(k,\theta\right), \tag{A17}$$

$$\gamma\left(k,\theta\right) = G\sqrt{B_{\mathrm{n}}}W, \tag{A18}$$

$$B_{\mathrm{n}} = A\left(k\right)N(k)\sigma k^{3}, \tag{A19}$$

$$W = \left(\frac{U}{c} - 1\right)^{2}. \tag{A20}$$

The directional distribution of W is implemented as the sum of favorable winds, $W_1 = \max^2\left\{0,\ \frac{U}{c}\cos(\theta-\theta_{\mathrm{w}})-1\right\}$, and adverse winds, $W_2 = \min^2\left\{0,\ \frac{U}{c}\cos(\theta-\theta_{\mathrm{w}})-1\right\}$. W is expressed as follows:

$$W = W_1 - a_0 W_2. \tag{A21}$$

The growth rate for adverse winds is negative; hence, in ST6, a negative input occurs in the parts of the wave spectrum where an adverse component of wind stress is present. This condition applies to the entire spectrum. In reality, a change in wind direction or invasion of remote swells would cause an opposing-wind wave component. Hence, this parameterization is expected to affect swell growth and dissipation. Wave-supported stress $\vec{\tau}_{\mathrm{w}}$ cannot exceed total stress $\vec{\tau}_{\mathrm{tot}}$, where $\vec{\tau}_{\mathrm{tot}} = \rho_{\mathrm{a}} u_* |u_*|$.

For dissipation caused by wave breaking, the threshold behavior and the cumulative dissipation effect are both parameterized following Rogers et al. (2012). The swell attenuation mechanism is parameterized in terms of the interaction of waves with oceanic turbulence (Babanin, 2011). This mechanism dominates at the front face of the spectrum.

$$S_{\mathrm{swl}}\left(k,\theta\right) = -\frac{2}{3} b_{\mathrm{l}} \sigma \sqrt{B_{\mathrm{n}}} N\left(k,\theta\right), \tag{A22}$$

where b_{l} is non-dimensional proportionality coefficient.